Super-resolution fluorescence imaging of carbon nanotubes using a nonlinear excitonic process

KEIGO OTSUKA,[1,2] **AKIHIRO ISHII,**[1,2] **AND YUICHIRO K. KATO**[1,2,*]

[1]*Quantum Optoelectronics Research Team, RIKEN Center for Advanced Photonics, Saitama 351-0198, Japan*
[2]*Nanoscale Quantum Photonics Laboratory, RIKEN Cluster for Pioneering Research, Saitama 351-0198, Japan*
[*]*yuichiro.kato@riken.jp*

Abstract: Highly efficient exciton-exciton annihilation process unique to one-dimensional systems is utilized for super-resolution imaging of air-suspended carbon nanotubes. Through the comparison of fluorescence signals in linear and sublinear regimes at different excitation powers, we extract the efficiency of the annihilation processes using conventional confocal microscopy. Spatial images of the annihilation rate of the excitons have resolution beyond the diffraction limit. We investigate excitation power dependence of the annihilation processes by experiment and Monte Carlo simulation, and the resolution improvement of the annihilation images can be quantitatively explained by the superlinearity of the annihilation process. We have also developed another method in which the cubic dependence of the annihilation rate on exciton density is utilized to achieve further sharpening of single nanotube images.

1.   Introduction

As a result of strong Coulomb interaction arising from the one-dimensional (1D) nature of single-walled carbon nanotubes (CNTs), electron-hole pairs form excitons that are stable even at room temperature [1–3]. When multiple excitons exist in a CNT, an exciton can scatter with another exciton and decay nonradiatively. In this Auger process known as exciton-exciton annihilation (EEA) [4–6], the exciton recombines by giving its energy to the other exciton. Confinement and diffusion [7–10] of the excitons in a nanotube lead to efficient EEA process upon collision with one another, resulting in a peculiar cubic dependence of the EEA rate on the density of excitons [11, 12]. The efficient EEA can be, for example, utilized in room-temperature single photon generation at telecommunication wavelengths [13, 14]. The diameter-dependent wavelength of nanotube fluorescence also includes the near-infrared window, where scattering is small and absorption is weak, allowing for deep-tissue imaging using CNTs as fluorescent agents [15–18]. As advanced techniques of super-resolution imaging [19–22], such as two-photon excitation microscopy and stimulated emission depletion microscopy, rely on the nonlinear optical response in fluorescence agents [23–28], the EEA process could play a key role in the development of nanotube-based biological imaging as well.

Here we demonstrate subdiffraction imaging of air-suspended CNTs by extracting the nonlinear EEA component using a typical confocal microscopy system. By combining two fluorescence images obtained at different excitation powers, an EEA rate image with enhanced resolution can be constructed. Excitation power-dependence of the extracted EEA efficiency and the spatial resolution of the EEA imaging are experimentally investigated, and we perform Monte Carlo simulation of the EEA process to identify the resolution limit of this technique. In addition to the use of nonlinearity between the EEA rate and the exciton generation rate, the cubic dependence of the EEA rate on exciton density is utilized in another protocol for super-resolution imaging of

CNTs. By measuring the excitation power required to establish a predefined exciton density, we are able to achieve even narrower widths for isolated nanotube images.

2. Air-suspended nanotubes and optical setup

The air-suspended nanotubes are synthesized by alcohol chemical vapor deposition [11, 29]. Trenches are formed on Si substrates through electron beam lithography and dry etching. We use Fe(III) acetylacetonate and fumed silica in ethanol as catalyst, where spin-coating and lift-off processes are used to deposit the catalyst in a region defined by another lithography process. After heating in air at 400°C for 5 min, CNTs are synthesized at 800°C for 1 min using Ar and H_2 flowing through an ethanol bubbler. A schematic and a scanning electron micrograph of an air-suspended nanotube are shown in Figs. 1(a) and 1(b), respectively.

A homebuilt confocal microscopy system is used to perform photoluminescence (PL) measurements at room temperature [11, 30–32]. A wavelength-tunable Ti:sapphire laser is used for excitation after controlling its power and polarization by neutral density filters and a half-wave plate, respectively. The laser beam is focused on the samples using an objective lens with a numerical aperture of 0.8 and a working distance of 3.4 mm. PL is collected through the same objective lens and detected using a liquid-nitrogen-cooled InGaAs diode array attached to a spectrometer. With the laser beam position fixed, we scan the samples mounted on a motorized three-dimensional stage to achieve focusing, sample search over the entire chip, and imaging of the single tubes. All measurements are performed in dry nitrogen to avoid formation of oxygen-induced defects [9, 33].
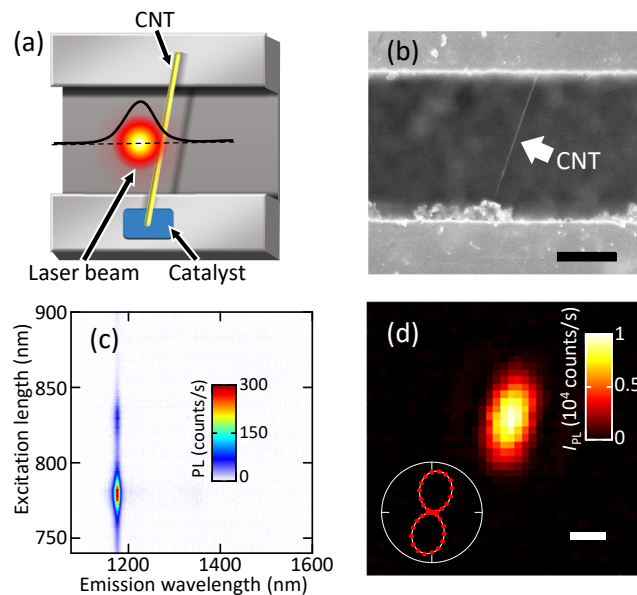

Fig. 1. (a) A schematic of an air-suspended nanotube sample. For optical imaging, the samples are scanned along trenches relative to the fixed laser beam. (b) A scanning electron micrograph of a typical nanotube. (c) A PL excitation map for a (11,3) nanotube. The excitation power is 0.1 μW. (d) A PL image of the nanotube measured in (c). Inset: Polarization dependence of I_{PL}. Excitation power and wavelength used for imaging are 0.1 μW and 780 nm, respectively, and the image is extracted at an emission wavelength of 1175 nm with a spectral integration window of ~50 nm. Scale bars in (b) and (d) are 500 nm.

3. Extraction of the influence of exciton-exciton annihilation

Figure 1(c) shows PL excitation spectroscopy data performed on a single air-suspended nanotube with a length $L \approx 1.2$ μm, and we determine the tube chirality to be (11,3). We then investigate laser polarization dependence of PL intensity with excitation energy at the E_{22} resonance [inset of Fig. 1(d)]. For the following PL measurements, the polarization angle and the excitation wavelength are fixed parallel to the tube axis and at the E_{22} resonance, respectively. Figure 1(d) shows an image of the integrated PL intensity I_{PL} obtained with a ~50-nm-wide spectral integration window centered at the E_{11} resonance. The width of the nanotube PL image is predominantly determined by the excitation laser beam profile, and thus much larger than the actual nanotube diameter of 1.0 nm.

The resolution enhancement will be achieved by using the efficient EEA process, whose effects can be observed in the power dependence of PL intensity [Fig. 2(a), black squares]. I_{PL} is proportional to the excitation power at low powers, but shows a cubic root dependence at high powers due to EEA [11]. The blue line in Fig. 2(a) is a linear fit to the low-power results, corresponding to the PL intensity expected in the absence of EEA. The deviation of actual PL intensity from the blue line would correspond to the EEA rate Γ_{EEA}.

The efficient EEA process also affects the imaging resolution. We measure 1D I_{PL} profiles of the nanotube along the trench direction with various excitation powers, and the full-width at half-maximum (FWHM) w_h of the profiles are plotted as red circles in Fig. 2(a) as a function of the excitation power. At the low power limit, PL intensity profiles reflect the excitation laser beam profile because I_{PL} is proportional to the exciton generation rate g in the absence of EEA. At the other extreme where I_{PL} is proportional to $g^{1/3}$ due to the cubic-law EEA process, we expect the effects of nonlinearity on the width of the PL intensity profile. If we approximate the laser beam profile by a Gaussian function $\exp(-2x^2/r^2)$ with r being the laser $1/e^2$ radius, the intensity profile of PL that has g^α dependence becomes $I_{PL}(x) \propto \exp(-2\alpha x^2/r^2) = \exp[-2x^2/(r/\sqrt{\alpha})^2]$, where α is the power exponent of the generation rate dependence. The FWHM changes by a factor

$$\frac{r/\sqrt{\alpha}\sqrt{2\ln 2}}{r\sqrt{2\ln 2}} = \frac{1}{\sqrt{\alpha}}, \tag{1}$$

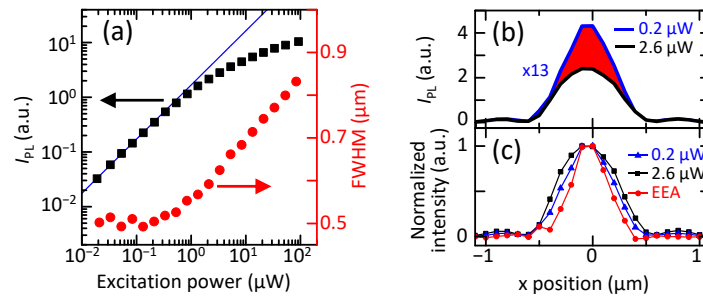and it is reasonable that the width of I_{PL} profile increases by a factor of $\sqrt{3}$ at the highest power.

Fig. 2. (a) Excitation power dependence of PL intensity I_{PL} with the laser focused at the center of the nanotube (black squares) and FWHM of PL intensity profiles along the trench direction (red circles). The nanotube is the same one as in Fig. 1(c) and 1(d). I_{PL} is obtained by calculating the peak area of a Lorentzian fit to the emission spectrum. (b) PL intensity profiles scaled by excitation powers. Difference of the black and the blue lines is proportional to the EEA rate Γ_{EEA}. (c) Normalized profiles of I_{PL} for the two different excitation powers and the EEA rate obtained from the subtraction in (b).

Although it may seem as if the EEA process has a negative effect on resolution, we can utilize the nonlinear power dependence on the generation rate to achieve enhanced spatial resolution. We extract the EEA component from PL intensities measured at two different excitation powers, where the EEA extraction power P_1 is higher than the reference power $P_2 = P_1/\kappa$, where $\kappa > 1$. Figure 2(b) illustrates how the EEA component is extracted. The black line is the PL intensity profile $I_{PL}(x, P_1 = 2.6~\mu W)$, showing slight broadening caused by EEA. The blue line is the intensity profile $I_{PL}(x, P_2 = 0.2~\mu W)$ scaled by κ, which is equivalent to the expected PL intensity profile in the absence of the EEA process. The difference between the black and blue lines $\kappa I_{PL}(x, P_2) - I_{PL}(x, P_1)$ (red region) is proportional to the EEA rate Γ_{EEA} in the nanotube.

Figure 2(c) shows normalized profiles of raw PL intensity (black and blue for P_1 and P_2, respectively) and the EEA component extracted by the protocol described above (red). The width of the intensity profile at the excitation power of $0.2~\mu W$ corresponds to the minimum width obtained in the power-dependent width in Fig. 2(a), but the profile of the extracted EEA component has an even smaller width. As Γ_{EEA} increases superlinearly with g, the spatial profile of the EEA component peaks sharply when the laser is centered on the nanotube.

To characterize the resolution and signal-to-noise ratio, we perform experiments using a range of excitation power combinations for extracting the EEA rate Γ_{EEA}. Measurements are repeated 7 times for each combination of the EEA extraction power P_1 and the reference power P_2, and the average width of the Γ_{EEA} profiles is plotted in Fig. 3(a) as a function of P_1 and P_2. Roughly speaking, large P_1 and P_2 result in large w_h of the Γ_{EEA} profiles, while low powers are preferable for high-resolution imaging.

We consider the widths obtained at the lowest $P_2 = 0.05~\mu W$ to quantitatively evaluate the resolution improvement. Figure 3(b) shows the P_1 dependence of w_h obtained from the raw PL intensity profiles (black squares) and the extracted EEA profiles with P_2 fixed at $0.05~\mu W$ (red circles). Error bars represent the standard deviation for the repeated measurements. The FWHM from raw PL reproduces the behavior observed in Fig. 2(a), and the error values are similar over the entire range of the excitation power. In comparison, the width for EEA rate profiles decreases from ∼500 to ∼350 nm as P_1 decreases, which is approximately an improvement by a factor of $\sqrt{2}$. We note that the width of the EEA profiles has large error bars at low powers because of the small Γ_{EEA} signals that depends superlinearly on g, becoming comparable to photon shot noise and detector noise.

4. Comparison with Monte Carlo simulation results

The minimum width achievable from the EEA profile in an ideal situation with negligible noise is investigated by conducting Monte Carlo simulation [11, 34] using parameters directly comparable with the experimental results. We use the same method as [11], and modify the excitation profile to reproduce the spatial scanning of the sample. Excitonic processes, such as exciton generation, diffusion, and decay, are evaluated at time intervals $\Delta t \leq 10^{-3}\tau$, where τ is the lifetime of the exciton intrinsic lifetime. For exciton generation, photons are supplied into the system at a rate with a spatial probability distribution given by a Gaussian function $\exp[-2(x^2 + y^2)/r^2]$, where x and y are positions perpendicular to and along the nanotube, respectively. Excitons are generated from the photons on the nanotube with a photon absorption width of 5 nm. Note that a width thicker than the physical width of the nanotube does not affect the following discussion based on the number of generated excitons $g\tau$, and it is used to reduce computational load. Probability for the exciton displacement s due to diffusion is given by the normal distribution $\frac{1}{\sqrt{4\pi D \Delta t}} \exp(-\frac{s^2}{4D\Delta t})$ with D being the diffusion constant. In addition to the intrinsic decay process that occurs with the probability of $\Delta t/\tau$, the excitons go through extrinsic decay (end quenching and EEA) after the diffusion. The tube length L and the laser radius r are $1.2~\mu m$ and $0.4~\mu m$, respectively, while the diffusion length $\sqrt{D\tau} = 1~\mu m$ is assumed.
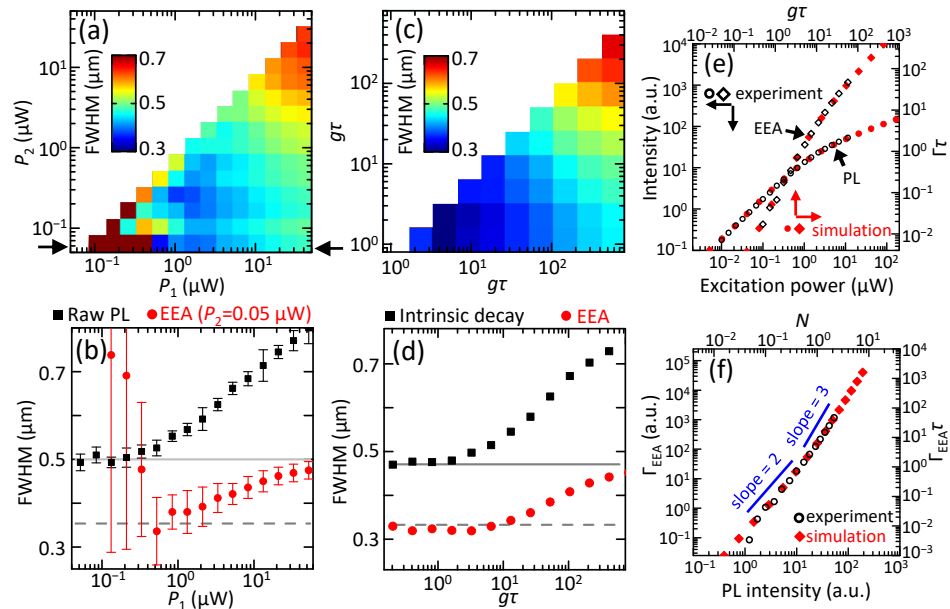
Fig. 3.   (a) FWHM of 1D EEA profiles as a function of the EEA extraction power P_1 and the reference power P_2 used for the subtraction of I_{PL}. The data are averaged for seven measurements repeated with the same condition. (b) FWHM of I_{PL} and the extracted EEA rate profiles for a fixed power of $P_2 = 0.05$ μW. Error bars represent the standard deviation. Solid and broken gray lines correspond to the laser beam FWHM and that multiplied by $1/\sqrt{2}$, respectively. (c) FWHM as a function of the EEA extraction and the reference generation rate from the Monte Carlo simulations. (d) FWHM of the intrinsic decay rate profiles and the EEA rate profiles from the simulations. (e) Excitation power dependence of the PL intensity and the extracted EEA component for the experiments and the simulations. (f) EEA rates as a function of I_{PL} and N from the experiments and the simulations, respectively.

1D rate profiles are calculated by moving the nanotube position in the x direction, simulating the experiment performed to obtain the I_{PL} profiles shown in Fig. 2(b). We compute the intrinsic decay rate Γ_I from the time-averaged number of excitons that go through the intrinsic decay, which corresponds to the PL intensity in the experiments. The simulations are repeated for various photon incident rates, and the EEA rate profiles are computed from Γ_I profiles in a manner similar to the measurements for Fig. 3(a). Figure 3(c) shows the FWHM of the extracted EEA rate profiles as a function of the EEA extraction and reference generation rates. Data are plotted in terms of a unitless parameter $g\tau$, representing the average number of excitons that are generated during τ. Note that we use the exciton generation rate evaluated with the nanotube at the center of the laser beam in Fig. 3, in which case it becomes equivalent to the excitation power in the experiments. The simulation results exhibit a trend similar to the experiments; large w_h for combinations of large $g\tau$ and vice versa.

Using the simulation data, it is possible to directly evaluate the EEA rates Γ_{EEA}. In Fig. 3(d), the FWHM of the EEA profiles as well as the intrinsic decay profiles are plotted, and both reproduce the overall behavior of the experimental data. As the generation rate is decreased, the width of the intrinsic decay approaches that of the simulated laser profile as indicated by the solid gray line. The EEA profile width, in comparison, is already below the solid line at large generation rates. The width decreases with the generation rate, and approaches the broken gray line which corresponds to $1/\sqrt{2}$ width of the laser profile. According to Eq. (1), the change in w_h

implies that the EEA rate has a nontrivial dependence on the exciton generation rate.

We experimentally confirm the g dependence of Γ_{EEA} by measuring the PL intensity [Fig. 3(e), open circles] and subtracting a linear fit to the low power PL data (open diamonds). Similarly, the $g\tau$ dependence of the intrinsic decay rate (filled circles) and the EEA rate (filled diamonds) obtained from the simulation is overlaid in Fig. 3(e) in terms of unitless parameters $\Gamma_I\tau$ and $\Gamma_{EEA}\tau$, respectively. The simulation is in good agreement with the experiment, showing that our simple model accurately describes the behavior of excitons in nanotubes. In this log-log plot, Γ_I has slopes of 1 and 1/3 at low and high generation rates, respectively, as also observed in Fig. 2(a). The slope of Γ_{EEA} is of our interest, which is 2 at low powers and approaches 1 as the power is increased. Through Eq. (1), the observed values of the slope can quantitatively explain the power dependence of w_h obtained from the EEA profiles [Fig. 3(d)].

The Γ_{EEA} slope of 1 at high power is reasonable, because $g \approx \Gamma_{EEA}$ with EEA being the dominant decay process. The quadratic dependence of Γ_{EEA}, however, seems to contradict with the cubic dependence expected for EEA [11]. In order to resolve this apparent inconsistency, $\Gamma_{EEA}\tau$ (filled diamonds) is plotted as a function of time-averaged exciton number $N = \Gamma_I\tau$ [Fig. 3(f)], and we find a transition from the quadratic to cubic dependence near $N = 1$. Similarly, the experimentally extracted EEA rate is replotted as a function of the PL intensity (open diamonds) in Fig. 3(f), which coincides with the simulation result. The transition in the N dependence of the EEA rate can be explained by the fact that EEA process occurs only when multiple excitons coexist in a nanotube. When $N > 1$ and the inter-exciton distance is small, the EEA rate in a 1D system is proportional to N^3 as discussed in [11]. When the exciton number $N \ll 1$, however, the situation changes. The probability for the instantaneous exciton number $\lambda \geq 3$ is negligible, while EEA does not occur for $\lambda = 0$ and 1. The EEA rate is then dominated by the case where two excitons coexist, whose probability is given by the Poisson distribution $p(\lambda) = N^\lambda e^{-N}/\lambda!$ to be $p(2) \approx N^2/2$. In this regime, multiple exciton generation, rather than exciton diffusion, is the limiting factor of the EEA process.

We can further obtain an explicit expression for the EEA rate. After time t from the first exciton generation, the survival probability of the first exciton and the arrival probability of the second exciton are $p_s(t) = \exp(-t/\tau)$ and $p_a(t) = gt\exp(-gt)$, respectively. The expectation value of the arrival time interval for when two excitons coexist is

$$\frac{\int_0^\infty t p_s(t) p_a(t) dt}{\int_0^\infty p_s(t) p_a(t) dt} = \frac{2\tau}{g\tau + 1} \approx 2\tau, \tag{2}$$

being independent of the exciton generation rate g as long as $N \ll 1$. The initial distance between the two excitons after diffusion is therefore constant ($\sim \sqrt{8D\tau/\pi}$). Despite the diffusion of the first exciton, the collision rate of such exciton pairs is then $\sim \pi/2\tau$ under the condition of $\lambda = 2$, and the EEA rate is given by

$$\Gamma_{EEA} \approx p(2) \times \frac{\pi}{2\tau} = \frac{\pi N^2}{4\tau}. \tag{3}$$

5. Two-dimensional images of exciton-exciton annihilation rates

Having understood the mechanism for the resolution improvement, we perform two-dimensional (2D) imaging of the raw PL intensity and the EEA rate. According to the analysis performed in Figs. 3(a) and 3(c), the reference power P_2 should be small enough to avoid EEA while the EEA extraction power P_1 also should be in the linear regime of I_{PL} vs the excitation power in order to obtain high resolution images. We note, however, that P_1 should not be too close to P_2 to keep the signal-to-noise ratio sufficiently high. We thus choose $P_1 = 0.8~\mu W$ and $P_2 = 0.1~\mu W$, where the excitation power is modulated by switching the neutral density filters at every step of the sample scan.
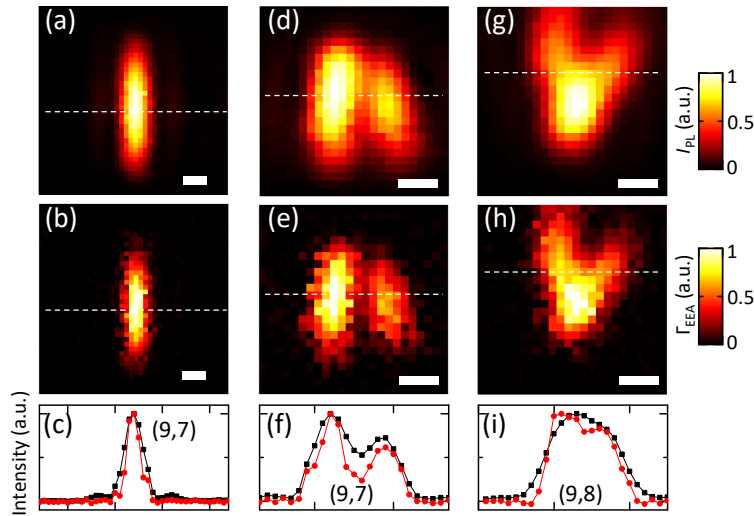
Fig. 4. 2D images of a (9,7) nanotube for (a) the PL intensity and (b) the extracted EEA rate. (c) 1D profiles from the PL (black) and EEA (red) images at the same position indicated by broken white lines. (d–i) Similar sets of 2D images and the 1D profiles for the two nanotubes with (d–f) a parallel and (g–i) a Y-shaped configuration. The excitation wavelengths are fixed at the E_{22} (784, 782, and 802 nm for (a–c), (d–f), and (g–i), respectively) of each nanotube, and all the images are extracted at the E_{11} wavelength (1284, 1290, and 1373 nm for (a–c), (d–f), and (g–i), respectively) with a spectral window of ~50 nm. All the images are normalized by their maximum intensity so that the image resolution can be easily compared. Scale bars are 500 nm.

Figure 4 displays the optical images for three configurations of nanotubes. Because $P_2 = 0.1\,\mu$W used for Figs. 4(a), 4(d), and 4(g) is in the linear regime of I_{PL}, the width of the raw PL image is solely limited by the laser beam profile and cannot be further reduced by lowering the power. In the simplest case of a single nanotube, the EEA image of the (9,7) nanotube [Fig. 4(b)] has even smaller width than the PL image [Fig. 4(a)]. We note that the EEA image represents the degree of PL intensity reduction through the EEA process. When two (9,7) tubes are lying closely, the tubes are more clearly resolved by extracting the EEA component, which is also apparent from the 1D profiles shown in Fig. 4(f). For a Y-shaped junction of (9,8) nanotubes, we show 1D profiles at the position where the I_{PL} profile of the two tubes cannot be resolved [black line in Fig. 4(i)]. These nanotubes are successfully separated through the super-resolution imaging of EEA rates.

The EEA imaging technique may potentially be applied to three-dimensional biological imaging. We expect similar resolution enhancement in the depth direction as the laser intensity profile along this axis can also be approximated by a Gaussian function. It is also worth mentioning that the nanotube lengths in the EEA images are slightly shortened because the EEA rate is small near the nanotube ends where the exciton density is low. In principle, the FWHM along the tube axis could become smaller than the diffraction limit by using short CNTs, though the resolution improvement would be quantitatively different from the other axes. It is noteworthy that the EEA-derived nonlinearity in nanotubes enables subdiffraction imaging at a power density as low as ~300 W/cm^2 with a continuous wave laser, whereas considerably higher intensities are employed for other subdiffraction techniques that utilize similar algorithms relying on PL saturation in dyes [26, 28]. We also note that this method is compatible with dispersed nanotubes used for biological imaging [15, 16, 18]. No modification of the protocol should be

needed, but the useful power range for EEA imaging will depend on the nanotube length and exciton diffusivity.

6. Image sharpening using the cubic-law excitonic process at high powers

We now consider whether it is possible to utilize the cubic dependence of the EEA rate Γ_{EEA} on N to achieve even higher resolution images. In the imaging protocol employed in Figs. 2–4, the g^2 dependence of Γ_{EEA} is used [Protocol I, left panel of Fig. 5(a)]. In comparison, we introduce a protocol that exploits the N^3 term of the EEA rate that appears at large N [Protocol II, right panel of Fig. 5(a)]. Instead of laser position dependent exciton generation rate $g(x)$ resulting from a constant excitation power in Protocol I, we create laser position dependent exciton number $N(x)$ that reproduces the laser beam profile. The EEA rate extracted from such $N(x)$ should allow for resolution enhancement through the cubic dependence. As briefly illustrated in Fig. 5(b), we first obtain a PL intensity profile $I_0(x)$ at a sufficiently low excitation power P_0 to purely extract the generation rate profile $g_0(x)$. Then $I_0(x)$ is multiplied by a constant $\kappa > 1$, which will be the target PL intensity $\kappa I_0(x)$ for the next scan. We reproduce the target PL intensity profile $\kappa I_0(x)$ by controlling the excitation power $P(x)$ to compensate for the intensity loss due to EEA. $P(x)$ is tuned at every point until the intensity difference between the measurement and $\kappa I_0(x)$ becomes less than 3%. The position-dependent exciton generation rate for this scan $g(x) = g_0(x)P(x)/P_0$ is used to extract the EEA rate $\Gamma_{EEA}(x)$. As the EEA rate is equal
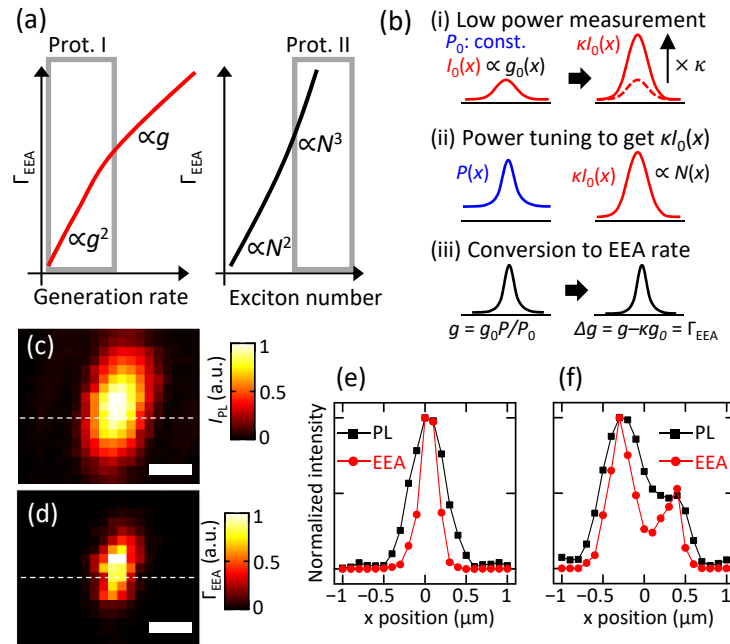

Fig. 5. (a) Illustration for utilizing the nonlinearity of Γ_{EEA} as a function of the exciton generation rate g or the exciton number N. While quadratic nonlinearity of Γ_{EEA} at small g is used for Protocol I (used in Figs. 2–4), cubic nonlinearity of Γ_{EEA} against N is used in Protocol II. (b) Schematics of the protocol to extract the cubic nonlinearity. (c) PL and (d) EEA images of the (11,3) nanotube with $P_0 = 0.2\ \mu W$ and $\kappa = 25$. Excitation and extraction wavelengths are 781 and 1176 nm, respectively. Scale bars are 500 nm. (e) 1D intensity profiles of the nanotube shown in (c) and (d). (f) Intensity profiles of the nanotubes shown in Figs. 4(d)–4(f). Excitation and extraction wavelengths are 780 and 1290 nm, respectively.

to the additional exciton generation rate compared with that expected in the absence of EEA, $\Gamma_{\text{EEA}}(x) = \Delta g(x) = g(x) - \kappa g_0(x)$.

Figures 5(c) and 5(d) show the raw PL image and the EEA rate image, respectively, obtained through Protocol II. Since larger κ gives smaller w_{h}, we choose $\kappa = 25$ and $P_0 = 0.2$ μW to fully utilize the N^3 nonlinearity at high powers, resulting in the maximum $P(x) = 53$ μW. Cross sectional profiles of these images are shown in Fig. 5(e). Clearly, the EEA rate image shows a narrower profile. If we take horizontal cross sections of the images and average the width along the length of the tube, the EEA image gives an average w_{h} of 290 nm, while that for the PL image is 520 nm. The width reduction corresponds to a factor of $\sqrt{3}$ as expected from the N^3 dependence. As shown in Fig. 5(f), this method can resolve multiple CNTs lying closely as a result of the improved spatial resolution. It should be noted, however, that the spatial resolution of the image does not always improve as much as the width observed for single tubes. Unlike the case in Protocol I, where the linear component of the PL is canceled out during the subtraction, the linear component from adjacent nanotubes is included in the signal during the power tuning step of Protocol II. The inclusion of the linear component inevitably causes a reduction of the nonlinear EEA component, resulting in a suboptimal resolution for high excitation powers.

7. Conclusion

In summary, we have performed super-resolution imaging of CNTs by visualizing the efficient EEA process using two protocols compatible with typical confocal microscopy systems. By subtracting the linear PL component to extract the nonlinear EEA rate, the spatial resolution improves by a factor of $\sqrt{2}$ compared to the diffraction limit. The resolution improvement is determined by the N^2 dependent EEA rate at low exciton numbers, as confirmed by Monte Carlo simulations. To utilize the N^3 dependence unique to the 1D system of nanotubes, we have developed another protocol for super-resolution imaging in which the excitation power is adaptively tuned during the measurement. Using the second protocol, the width of a single nanotube can be as narrow as $1/\sqrt{3}$ compared to the conventional PL imaging. The absorption and emission at the near-infrared window and the nonlinear response that appears at low excitation density would open up a pathway for the resolution enhancement in applications such as deep tissue imaging with suppressed damages.

Disclosures

The authors declare that there are no conflicts of interest related to this article.

References

1. T. Ogawa and T. Takagahara, "Optical absorption and sommerfeld factors of one-dimensional semiconductors: An exact treatment of excitonic effects," Phys. Rev. B **44**, 8138–8156 (1991).
2. T. Ando, "Excitons in carbon nanotubes," J. Phys. Soc. Jpn. **66**, 1066 (1997).
3. F. Wang, G. Dukovic, L. E. Brus, and T. F. Heinz, "The optical resonances in carbon nanotubes arise from excitons," Science **308**, 838–841 (2005).
4. F. Wang, G. Dukovic, E. Knoesel, L. E. Brus, and T. F. Heinz, "Observation of rapid Auger recombination in optically excited semiconducting carbon nanotubes," Phys. Rev. B **70**, 241403 (2004).

5. Y.-Z. Ma, L. Valkunas, S. L. Dexheimer, S. M. Bachilo, and G. R. Fleming, "Femtosecond spectroscopy of optical excitations in single-walled carbon nanotubes: Evidence for exciton-exciton annihilation," Phys. Rev. Lett. **94**, 157402 (2005).
6. Y.-F. Xiao, T. Q. Nhan, M. W. B. Wilson, and J. M. Fraser, "Saturation of the photoluminescence at few-exciton levels in a single-walled carbon nanotube under ultrafast excitation," Phys. Rev. Lett. **104**, 017401 (2010).
7. Y. Murakami and J. Kono, "Existence of an upper limit on the density of excitons in carbon nanotubes by diffusion-limited exciton-exciton annihilation: Experiment and theory," Phys. Rev. B **80**, 035432 (2009).
8. S. Moritsubo, T. Murai, T. Shimada, Y. Murakami, S. Chiashi, S. Maruyama, and Y. K. Kato, "Exciton diffusion in air-suspended single-walled carbon nanotubes," Phys. Rev. Lett. **104**, 247402 (2010).
9. K. Yoshikawa, K. Matsuda, and Y. Kanemitsu, "Exciton transport in suspended single carbon nanotubes studied by photoluminescence imaging spectroscopy," J. Phys. Chem. C **114**, 4353–4356 (2010).
10. J. Xie, T. Inaba, R. Sugiyama, and Y. Homma, "Intrinsic diffusion length of excitons in long single-walled carbon nanotubes from photoluminescence spectra," Phys. Rev. B **85**, 085434 (2012).
11. A. Ishii, M. Yoshida, and Y. K. Kato, "Exciton diffusion, end quenching, and exciton-exciton annihilation in individual air-suspended carbon nanotubes," Phys. Rev. B **91**, 125427 (2015).
12. S. Khasminskaya, F. Pyatkov, K. Słowik, S. Ferrari, O. Kahl, V. Kovalyuk, P. Rath, A. Vetter, F. Hennrich, M. M. Kappes, G. Gol'tsman, A. Korneev, C. Rockstuhl, R. Krupke, and W. H. P. Pernice, "Fully integrated quantum photonic circuit with an electrically driven light source," Nat. Photon. **10**, 727–732 (2016).
13. X. Ma, O. Roslyak, J. G. Duque, X. Pang, S. K. Doorn, A. Piryatinski, D. H. Dunlap, and H. Htoon, "Influences of exciton diffusion and exciton-exciton annihilation on photon emission statistics of carbon nanotubes," Phys. Rev. Lett. **115**, 017401 (2015).
14. A. Ishii, T. Uda, and Y. K. Kato, "Room-temperature single-photon emission from micrometer-long air-suspended carbon nanotubes," Phys. Rev. Appl. **8**, 054039 (2017).
15. G. Hong, J. C. Lee, J. T. Robinson, U. Raaz, L. Xie, N. F. Huang, J. P. Cooke, and H. Dai, "Multifunctional in vivo vascular imaging using near-infrared II fluorescence," Nat. Med. **18**, 1841–1846 (2012).
16. Y. Yomogida, T. Tanaka, M. Zhang, M. Yudasaka, X. Wei, and H. Kataura, "Industrial-scale separation of high-purity single-chirality single-wall carbon nanotubes for biological imaging," Nat. Commun. **7**, 12056 (2016).
17. S. Aota, N. Akizuki, S. Mouri, K. Matsuda, and Y. Miyauchi, "Upconversion photoluminescence imaging and spectroscopy of individual single-walled carbon nanotubes," Appl. Phys. Express **9**, 045103 (2016).
18. N. Danné, A. G. Godin, Z. Gao, J. A. Varela, L. Groc, B. Lounis, and L. Cognet, "Comparative analysis of photoluminescence and upconversion emission from individual carbon nanotubes for bioimaging applications," ACS Photonics **5**, 359–364 (2017).
19. M. J. Rust, M. Bates, and X. Zhuang, "Sub-diffraction-limit imaging by stochastic optical reconstruction microscopy (STORM)," Nat. Methods **3**, 793–796 (2006).
20. L. Cognet, D. A. Tsyboulski, and R. B. Weisman, "Subdiffraction far-field imaging of luminescent single-walled carbon nanotubes," Nano Lett. **8**, 749–753 (2008).
21. S. W. Hell, S. J. Sahl, M. Bates, X. Zhuang, R. Heintzmann, M. J. Booth, J. Bewersdorf, G. Shtengel, H. Hess, P. Tinnefeld, A. Honigmann, S. Jakobs, I. Testa, L. Cognet, B. Lounis, H. Ewers, S. J. Davis, C. Eggeling, D. Klenerman, K. I. Willig, G. Vicidomini, M. Castello, A. Diaspro, and T. Cordes, "The 2015 super-resolution microscopy roadmap," J. Phys. D: Appl. Phys. **48**, 443001 (2015).
22. N. Danné, M. Kim, A. G. Godin, H. Kwon, Z. Gao, X. Wu, N. F. Hartmann, S. K. Doorn, B. Lounis, Y. Wang, and L. Cognet, "Ultrashort carbon nanotubes that fluoresce brightly in the near-infrared," ACS Nano **12**, 6059–6065 (2018).
23. W. Denk, J. H. Strickler, and W. W. Webb, "Two-photon laser scanning fluorescence microscopy," Science **248**, 73–76 (1990).
24. S. W. Hell and J. Wichmann, "Breaking the diffraction resolution limit by stimulated emission: stimulated-emission-depletion fluorescence microscopy," Opt. Lett. **19**, 780–782 (1994).
25. R. Heintzmann, T. M. Jovin, and C. Cremer, "Saturated patterned excitation microscopy—a concept for optical resolution improvement," J. Opt. Soc. Am. A **19**, 1599–1609 (2002).
26. K. Fujita, M. Kobayashi, S. Kawano, M. Yamanaka, and S. Kawata, "High-resolution confocal microscopy by saturated excitation of fluorescence," Phys. Rev. Lett. **99**, 228105 (2007).
27. A. Chmyrov, J. Keller, T. Grotjohann, M. Ratz, E. d'Este, S. Jakobs, C. Eggeling, and S. W. Hell, "Nanoscopy with more than 100,000 'doughnuts'," Nat. Methods **10**, 737–740 (2013).
28. Y. Zhang, P. D. Nallathamby, G. D. Vigil, A. A. Khan, D. E. Mason, J. D. Boerckel, R. K. Roeder, and S. S. Howard, "Super-resolution fluorescence microscopy by stepwise optical saturation," Biomed. Opt. Express **9**, 1613–1629 (2018).
29. S. Maruyama, R. Kojima, Y. Miyauchi, S. Chiashi, and M. Kohno, "Low-temperature synthesis of high-purity single-walled carbon nanotubes from alcohol," Chem. Phys. Lett. **360**, 229–234 (2002).
30. M. Jiang, Y. Kumamoto, A. Ishii, M. Yoshida, T. Shimada, and Y. K. Kato, "Gate-controlled generation of optical pulse trains using individual carbon nanotubes," Nat. Commun. **6**, 6335 (2015).
31. T. Uda, M. Yoshida, A. Ishii, and Y. K. Kato, "Electric-field induced activation of dark excitonic states in carbon nanotubes," Nano Lett. **16**, 2278–2282 (2016).
32. N. Higashide, M. Yoshida, T. Uda, A. Ishii, and Y. K. Kato, "Cold exciton electroluminescence from air-suspended

carbon nanotube split-gate devices," Appl. Phys. Lett. **110**, 191101 (2017).
33. C. Georgi, N. Hartmann, T. Gokus, A. A. Green, M. C. Hersam, and A. Hartschuh, "Photoinduced luminescence blinking and bleaching in individual single-walled carbon nanotubes," Chem. Phys. Chem. **9**, 1460–1464 (2008).
34. S. Mouri, Y. Miyauchi, M. Toh, W. Zhao, G. Eda, and K. Matsuda, "Nonlinear photoluminescence in atomically thin layered WSe_2 arising from diffusion-assisted exciton-exciton annihilation," Phys. Rev. B **90**, 155449 (2014).